Vesuvianite: A potential U-Pb geochronometer for skarn mineralization---a case study of tungsten and tin deposits in South China

Langzhang Xing [a,b], Jiantang Peng [a,c,*], Yuanjun Lv [a,b], Yanwen Tang [a], Jianfeng Gao [a]

[a] State Key Laboratory of Ore Deposit Geochemistry, Institute of Geochemistry, Chinese Academy of Sciences, Guiyang 550081, China
[b] College of Earth and Planetary Sciences, University of Chinese Academy of Sciences, Beijing 100049, China
[c] School of Geosciences and Info-Physics, Central South University, Changsha 410083, China

ARTICLE INFO

ABSTRACT

Vesuvianite is one kind of common U-bearing minerals in various skarns and skarn mineralization. As an early phase mineral, vesuvianite can be well preserved since it usually occurs at the front of skarn close to the marble and far away from the pluton, therefore, accurately determining its growth history can directly date hydrothermal activity in the skarn system, just like the zircon U-Pb geochronometer recording magmatic processes. In order to demonstrate reliability of the vesuvianite U-Pb geochronometer, we choose six vesuvianite samples from two skarn deposits in South China for the LA-ICPMS dating. Accordingly, the U-Pb dating of four vesuvianite samples from the Shizhuyuan W-Sn ore district yielded precise ages of 160.3 $\pm$ 1.2 Ma, 155.6 $\pm$ 2.6 Ma, 154.5 $\pm$ 3.1 Ma and 150.4 $\pm$ 3.1 Ma, respectively; these dates coincide well with the previously published ages of the relevant granite complex emplacement and hydrothermal mineralization in the region with the ages of ca. 160 Ma, ca. 155 Ma and ca. 150 Ma. The other two vesuvianite samples from the Furong Sn ore district yielded precise ages of 159.3 $\pm$ 1.8 Ma and 149.1 $\pm$ 1.6 Ma, which are consistent with the multi-stage magmatic activities in the studied area with emplacement time of ca. 160 Ma and ca. 149 Ma. Theoretically, the site of the Ca^{2+} position in vesuvianite is slightly larger than that in intergrown grossularite, which gives the former a better ability to incorporate uranium. Therefore, vesuvianite with high uranium concentrations and relatively low common Pb is beneficial for obtaining precise results during the LA-ICPMS U-Pb dating, it is an ideal mineral for accurately determining the time of skarn formation and/or various skarn mineralization.

1. Introduction

Skarn deposits are one of the most important ore types in the continental crust which provide major sources for various metals (including Sn, W, Cu, Au, Ag, Mo, Zn-Pb and Fe) and can be formed in carbonates of almost all ages (Einaudi and Burt, 1982; Meinert et al., 2005). In China, the most important 386 skarn deposits contain about 8.9 Mt Sn (87% of China's Sn resources, hereinafter given in 87%), 6.6 Mt WO$_3$ (71%), 42 Mt Cu (32%), 81 Mt Zn + Pb (25%), 5.4 Mt Mo (17%), 1871 t Au (11%), 42,212 t Ag (10%), and about 8500 Mt high-grade Fe ores (ca. 9%) (Chang et al., 2019), making them an extremely important source of many metals.

Although there are extensive studies about skarn deposits, the exact mineralization ages of many skarn deposits remain controversial. Many researches usually inferred the mineralization time indirectly by determining the emplacement age of related intrusions (Seman et al., 2017).

However, for those complex intrusions formed by multiple magmatic activities, the observable crosscutting or contact relationship do not support the intrinsic associations between intrusions and skarn deposits (Seman et al., 2017). Many direct dating methods have been exploited during the past several decades by dating ore minerals or skarn minerals, including (but not limited) the Re-Os dating of molybdenite, pyrite and arsenopyrite (e.g., Luck and Allègre, 1982; Mathur et al., 1999; Stein et al., 2000; Yu et al., 2005), U-Pb dating of titanite, cassiterite and garnet (e.g., Tilton and Grünenfelder, 1968; Gulson and Jones, 1992; Deng et al., 2017; Seman et al., 2017), but these minerals are not always present, or do not yield accurate ages, even fail to obtain any geologically meaningful dates due to the extremely low concentrations for the parent element.

During the analysis of the trace elements for garnet and vesuvianite, we found that vesuvianite may have high uranium concentration and relatively low lead concentration when uranium is available in the

hydrothermal system, which made us realize that vesuvianite should have the potential for U-Pb dating, and its coarse-grained macroscopic features also make it easier to be sampled and performed for the LA-ICPMS analysis. Actually, as a common hydrous silicate of calcium and aluminum in various skarns, vesuvianite has been successfully used for U-Pb dating by the ID-TIMS method in the 1990s (Romer, 1992). However, little attention had been paid on this mineral after Romer's innovative attempt. Recently, another research team also exploits the vesuvianite LA-ICPMS U-Pb dating method using garnet as primary standard (Wei et al., 2022).

In this study, we carry out the in-situ LA-ICPMS U-Pb isotopic dating by using zircon 91500 as primary standard on vesuvianite samples from the giant Shizhuyuan W-Sn and Furong Sn deposits in the Nanling region, South China (Fig. 1). Both deposits have been studied in detail during the past several decades, a lot of dates previously published on the hydrothermal mineralization and the related intrusion emplacement, will help us to judge whether the vesuvianite ages obtained here

are accurate, and finally to evaluate the reliability of this new dating method. Also, we briefly discuss the geochemical behavior of uranium and lead in vesuvianite, and attempt to theoretically elucidate why vesuvianite exhibits a strong capacity to accommodate uranium, which is beneficial to the LA-ICPMS U-Pb dating.

2. Geological setting

2.1. Regional geology

The Nanling region is extraordinarily rich in tungsten and tin resources, with about 7.69 Mt WO_3 and 2.39 Mt Sn, approximately accounts for 74.7% and 52.6% of total resources in China (Wang et al., 2020). The Nanling region can be delineated within 111°–116° E and 27°–24° N with the exposed area about 150,000 km^2 (Shu et al., 2006; Fig. 1). The basement strata in the Nanling region are composed of Precambrian to Paleozoic clastic sedimentary rocks and meta-
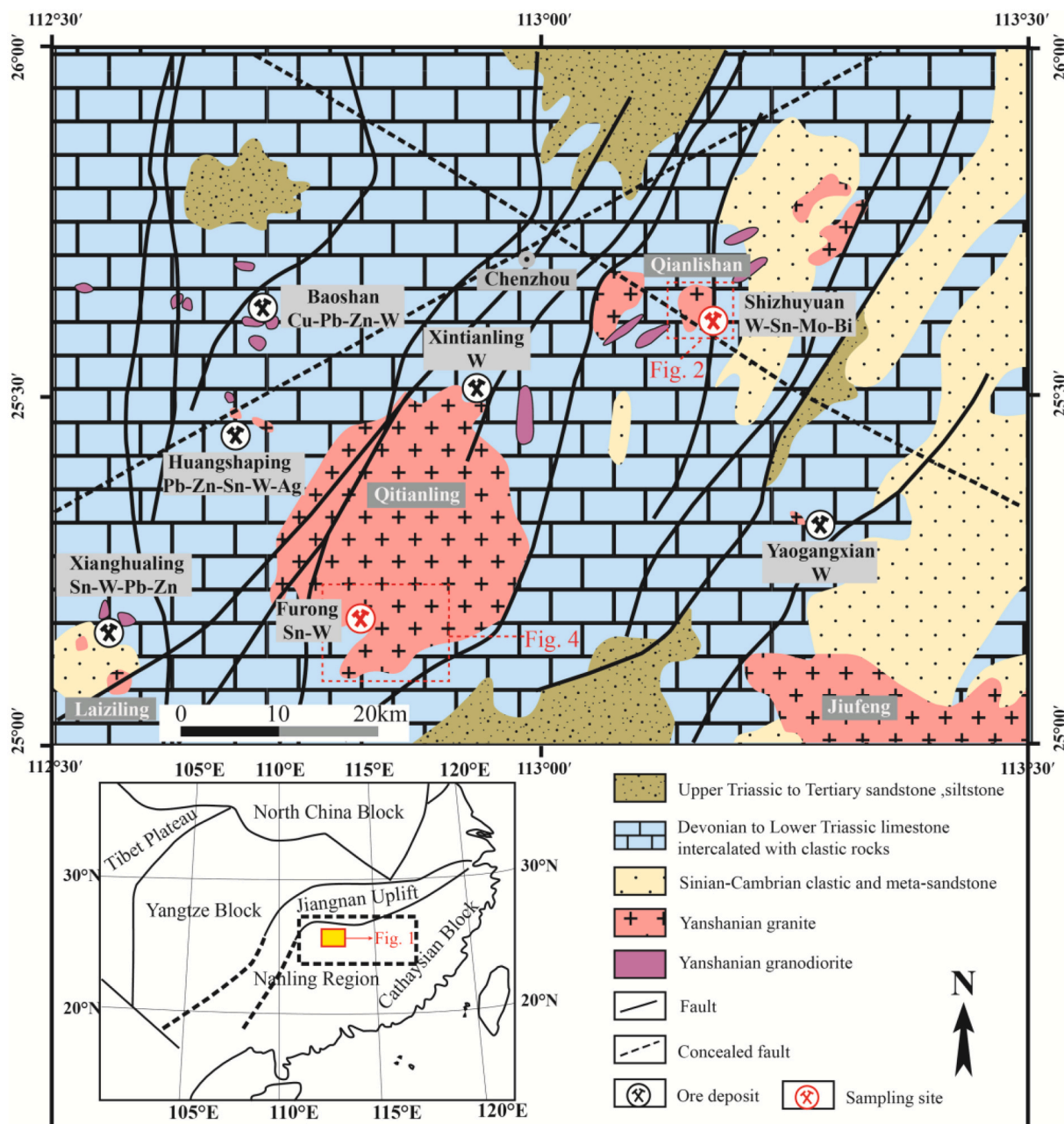

Fig. 1. Simplified geological map of central Nanling region, South China, and distribution of mineral deposits in the studied region. Modified after Peng et al. (2006).

sedimentary rocks, and experienced intense deformation during the Silurian orogeny (Zhang et al., 2013; Shu et al., 2006, 2020). The Devonian to Triassic carbonate rocks and clastic sedimentary rocks constitute the cover strata, together with the basement, it underwent intense deformation during the Triassic orogeny, and further re-deformed during the Jurassic-Cretaceous and Tertiary orogeny (Zhang et al., 2013; Shu et al., 2006, 2020). The granitic magmatic activities are widespread throughout the Nanling region, mainly including the late Paleozoic, the early and late Mesozoic (Chen et al., 1989; Zhang et al., 2013), among them, the Jurassic-Cretaceous magmatism is the most important, which contributes to the large-scale W-Sn mineralization in the Nanling region (Chen et al., 1989; Mao et al., 2007, 2013; Peng et al., 2008).

2.2. Shizhuyuan W-Sn deposit

The Shizhuyuan W-Sn polymetallic deposit, with the metal reserves of 0.75 Mt WO_3, 0.49 Mt Sn, 0.3 Mt Bi, 0.13 Mt Mo and 0.2 Mt Be (Lu et al., 2003), is a worldclass giant deposit. The stratigraphic sequence in the deposit includes Sinian, Devonian, Carboniferous, Jurassic and Cretaceous sedimentary rocks. The skarn and related metallic mineralization mainly occur at the contact zone between the Middle to Upper Devonian limestone and the Qianlishan pluton (Wang et al., 1987). The causative Qianlishan pluton crops out over 10 km^2 and consists of

multiple granitic phases. According to the field observations, petrological characteristics and geochronological data, the Qianlishan granitic complex can be roughly sub-divided into four emplacement phases (Fig. 2). (1) The first emplacement at ca. 160 to 158 Ma (Chen et al., 2014; Chen et al., 2016), is located at the outer part of the Qianlishan complex and is predominantly composed of fine- to medium-grained porphyritic biotite granite (Wang et al., 1987); (2) The second emplacement at ca. 156 to154 Ma (Chen et al., 2014; Chen et al., 2016; Zhao et al., 2018; Jiang et al., 2019; Liao et al., 2021), occurring in the central part of the pluton and outcrops over 5.6 km^2 (Wang et al., 1987), is mainly composed of medium- to coarse-grained equigranular biotite granite (Wang et al., 1987). There are some unexposed fine- to medium-grained equigranular biotite granites in the Ma'naoshan and Congshuban districts which were intruded by the NE-trending granite porphyry dykes. These unexposed plutons are also emplaced at ca. 155 Ma (Zhao et al., 2018). (3) The third emplacement at ca. 152 to 150 Ma (Guo et al., 2015; Jiang et al., 2019) occurs in the southern of the Qianlishan pluton on a small scale, and is mainly composed of the fine-grained two mica granite, quartz and granite porphyries. (4) The fourth pluton emplaced at 146 to 142 Ma, is mainly made up of diabase and granite porphyry dykes (Liu et al., 1997), and some of them intruded into the earlier granites (Wang et al., 1987). Noticeably, the first and second emplacements constitute the main body of the Qianlishan granite, and the third and fourth intrusions form the granite complement.
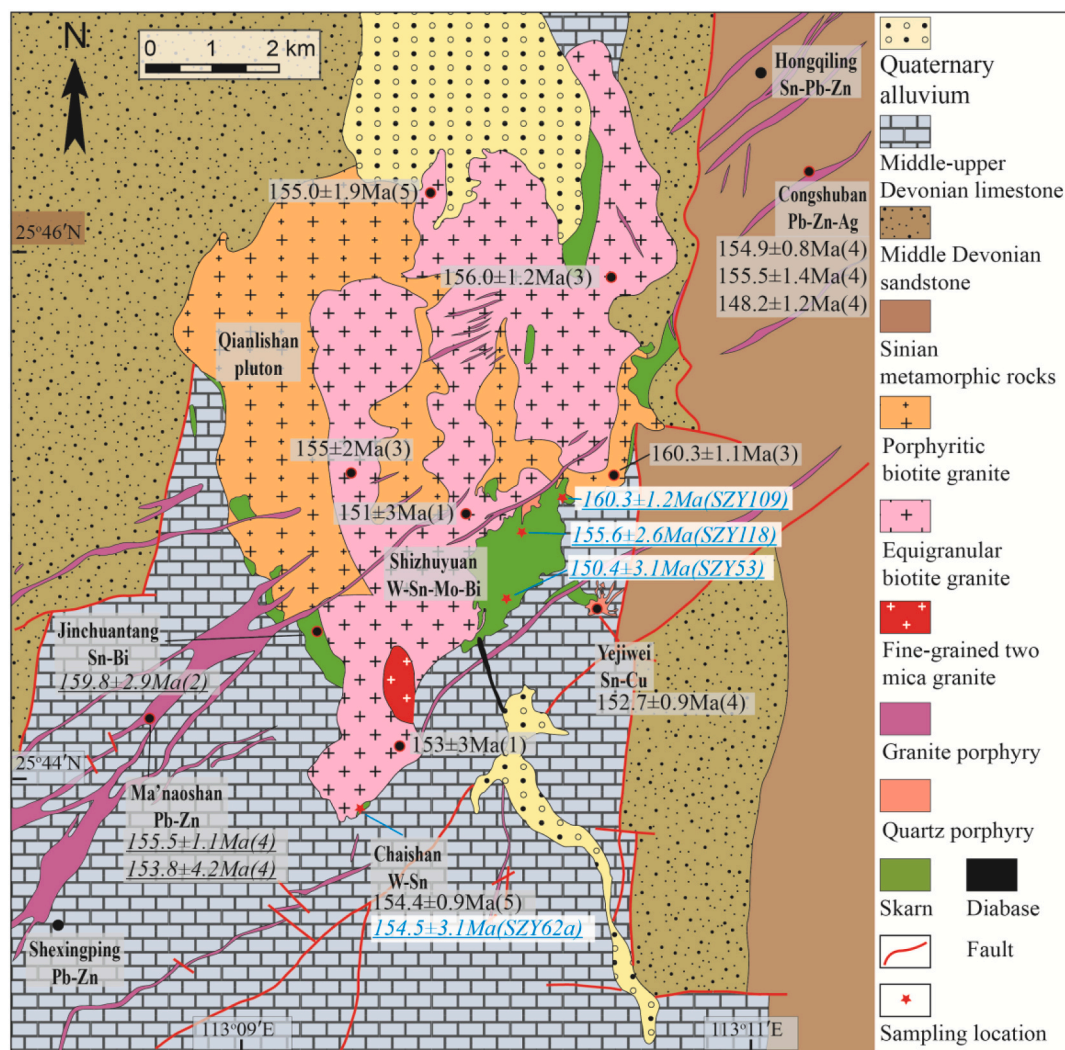

Fig. 2. Geological map of the Qianlishan complex and the Shizhuyuan W-Sn deposit, South China. Modified after Wang et al. (1987). References of the dates: (1) Li et al., 2004; (2) Liu et al., 2012; (3) Chen et al., 2014; (4) Zhao et al., 2018; (5) Liao et al., 2021.

Skarn and greisen mineralization predominate in the Shizhuyuan deposit. As the most important mineralization type, the skarns in this region are mineralogically heterogeneous, and exhibit typical mineral assemblage zoning. The zoning from the granite contact outward includes garnet skarn, pyroxene-garnet skarn, garnet-pyroxene skarn, laminated garnet-pyroxene skarn, garnet-bearing wollastonite-vesuvianite skarn, vesuvianite-bearing wollastonite skarn, argillaceous striped marble, and massive marble, respectively (Wang et al., 1987; Mao et al., 1996). Greisen is also widespread in the deposit and includes massive and fracture-controlled stockwork types; the massive greisen mainly occurs in the upper part of altered granites, the fracture-controlled greisen veins and veinlets usually appear as layers and lenses with several hundred meters in length and tens of meters in width, and can cut both skarn and massive greisen (Lu et al., 2003). Gangue minerals mainly include quartz, topaz, plagioclase, muscovite, lepidolite, and fluorite, and ore minerals are mainly scheelite, wolframite, molybdenite, bismuthinite and cassiterite (Wang et al., 1987; Mao et al., 1996; Lu et al., 2003). Four types of mineralization can be distinguished in the studied deposit according to their composition, texture, structure and mining terminology (Wang et al., 1987; Lu et al., 2003; Fig. 3): (1) Sn-Be veinlet mineralization in marble and sericitic porphyry; (2) W-Bi-Mo massive skarn mineralization; (3) W-Sn-Mo-Bi-F stockwork mineralization overprinting on skarn and partly on greisen; (4) W-Sn-Mo-Bi massive greisen mineralization.

2.3. Furong tin deposit

The Furong tin deposit with the estimated Sn reserves of about 0.7 Mt and an average ore grade of 0.3–1.5% Sn (Huang et al., 2001), located in the southern margin of the Qitianling granite batholith in southern Hunan Province, is the largest one throughout the Nanling region and ranks the third among skarn tin deposits in China (Chang et al., 2019). The exposed strata in the deposit mainly consist of Carboniferous to Permian carbonates with silty, siliceous and calcareous shale, unconformable overlain by Cretaceous red beds. Tin mineralization predominately occurs in the Lower Permian and Lower Carboniferous carbonates (Huang et al., 2001). The causative Qitianling granite batholith crops over 520 km^2 and is the largest intrusion throughout the southern Hunan province. Field observations, petrological characteristics and geochronological data indicate that the Qitianling granite
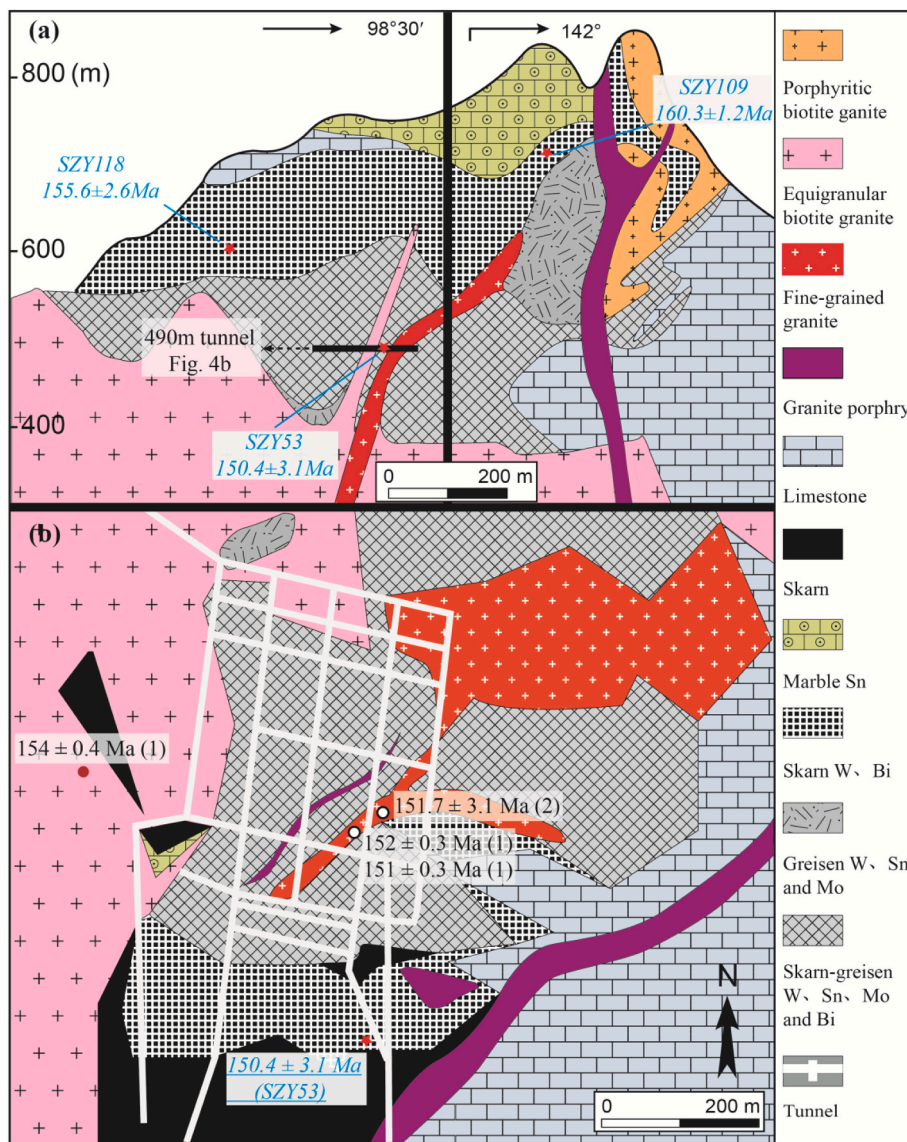

Fig. 3. (a) Profile of the Shizhuyuan deposit, showing the distribution of the four main ore types. The orientation of the first part of the profile is 98°30′; the second part is oriented 142° (Modified after Wang et al., 1987, Lu et al., 2003). (b) Geologic map of the level 490 m tunnel (Modified after Wang et al., 1987 and Lu et al., 2003). References of the dates: (1) Jiang et al., 2019; (2) Liao et al., 2021.

belongs to an early Mesozoic complex batholith. The detailed zircon U-Pb geochronological studies for the granite complex have revealed that the magmatic emplacement responsible for this complex spans a period of 163 Ma to 145 Ma and at least includes four discrete pulses of igneous activities (Fig. 4). (1) The first emplacement at ca. 163 to 160 Ma, with a peak at ca. 160 Ma (Fu et al., 2004; Zhu et al., 2009), occurs in the eastern, northern, and western peripheral parts of the pluton and is composed predominantly of medium- to coarse-grained porphyritic hornblende biotite monzonitic granite. (2) The second emplacement at ca. 157 to 155 Ma (Li et al., 2005; Li et al., 2006; Zhao et al., 2006; Zhu et al., 2009), is distributed in the central and southeastern parts of the pluton, and is mainly composed of medium- to coarse-grained porphyritic biotite (locally with few hornblende) granite. (3) The third emplacement at ca. 150 to 149 Ma (Zhu et al., 2009), occurs in the south-central part of the pluton and is mainly composed of fine-grained (locally porphyritic) biotite granites. (4) The fourth emplacement at 146 to 145 Ma are granite porphyry dykes which intrude into earlier granite locally (Li et al., 2006). The first and second emplacements constitute the major phase of the Qitianling granite batholith, and the third and fourth intrusions make up its complement phase.

Orebodies are hosted mainly within granite or at the contact zone between the granite and carbonate rocks (Huang et al., 2001). More than 50 ore veins have been delineated in the deposit, which can be divided into Shanmenkou-Taoxiwo-Goutouling, Heishanli-Maziping and Bailashui-Anyuan ore belts from SE to NW (Fig. 4). The mineralization

types mainly include skarn, altered granite and greisen types. The Bailashui-Anyuan ore belt is mainly characterized by skarn and altered granite mineralization, while the Heishanli-Maziping and the Shanmenkou-Taoxiwo-Goutouling ore belts are predominated by greisen mineralization. Among them, the Bailashui-Anyuan ore belt is the largest, whose reserves contributes about 72.4% of the total Sn resources in the Furong deposit, and No. 19 orebody is the largest one in the Bailashui-Anyuan ore belt with ca. 0.27 Mt Sn and an average grade of 0.79% Sn (Cai et al., 2004). No.19 orebody occurs at the contact zone between the carbonate rocks and the granitic intrusion, and there both endoskarn and exoskarn are well developed (Fig. 4); the exoskarn is mainly composed of diopside, andradite-grossularite, vesuvianite, wollastonite, with minor quartz and fluorite; and the endoskarn mainly consists of epidote and orthoclase, with a small amount of diopside and grossularite, and displays zonation of mineral assemblages (Mao et al., 2004). Locally, phlogopite rocks occur in skarn of No.19 orebody (Peng et al., 2007).

3. Sampling and analytical methods

3.1. Sampling locations

In this study, four vesuvianite samples were collected from Shizhuyuan deposit. Samples SZY109 and SZY118 were collected from the open pits (Fig. 2), the sample SZY109 was taken from the skarn
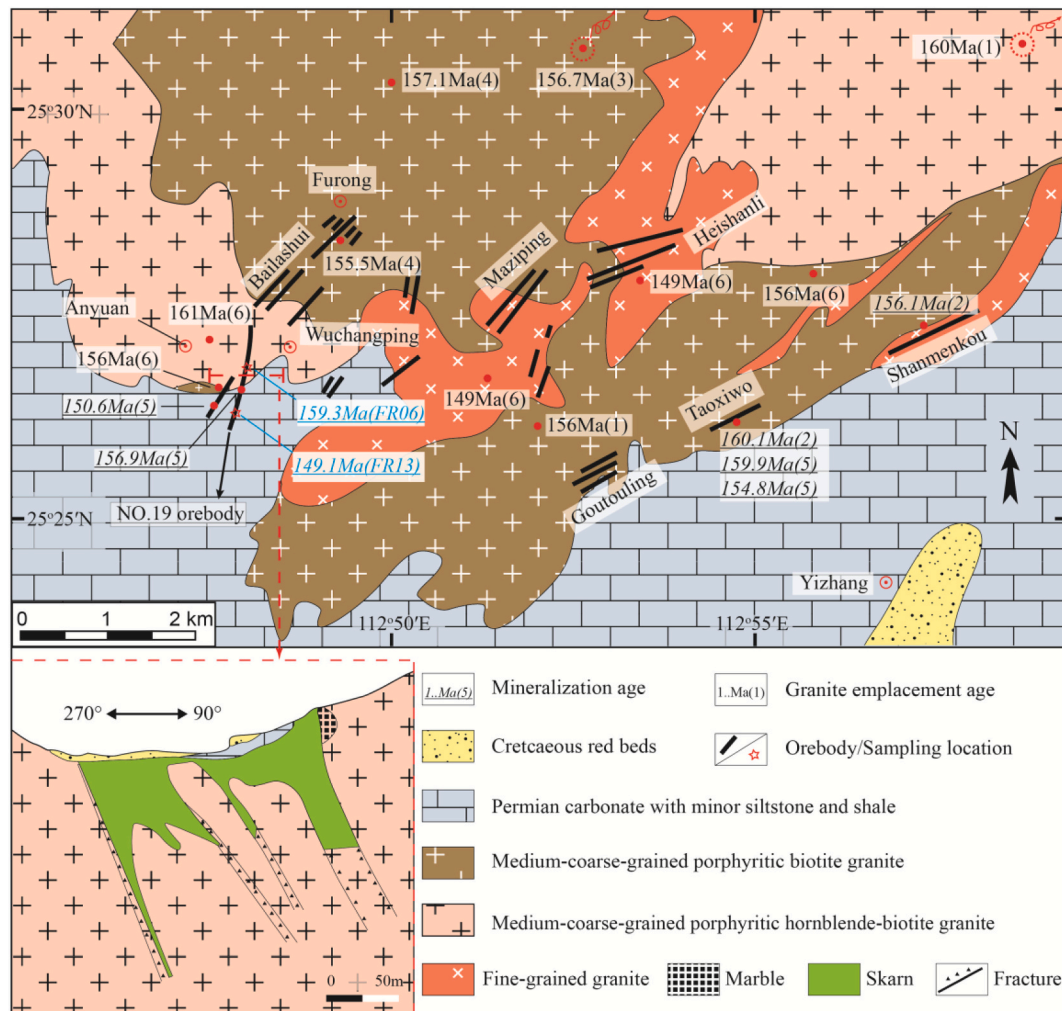

Fig. 4. Geological map of the Qitianling complex and the Furong tin deposit, South China. Modified after Mao et al. (2004) and Zhu et al. (2009). References of the dates: (1) Fu et al., 2004; (2) Mao et al., 2004; (3) Li et al., 2005; (4) Zhao et al., 2006; (5) Peng et al., 2007; (6) Zhu et al., 2009.

outcropping between the earliest granite and the limestone with the altitude of ca. 690 m, and the sample SZY118 was taken from the skarn occurring between the second granite and the limestone with the altitude of 591 m. Sample SZY53 was taken from skarn in the 490 m level tunnel (Fig. 3), and Sample SZY62 was taken from the Chaishan pit located between the second granite and the limestone in the same deposit (Fig. 2). The other two samples were all collected from No.19 orebody in the Furong deposit (Fig. 4), Sample FR06 was taken from the skarn between the earliest granite and the limestone, Sample FR13 was also collected from skarn ores, but its contact relationship with the causative granite is still unclear.

3.2. Analytical methods

Minerals in the skarn samples collected in this study are predominated by grossularite, vesuvianite and wollastonite, with less fluorite, calcite, quartz and scheelite (Fig. 5). Vesuvianite usually occurs in the form of nearly euhedral columnar or radiating bright green aggregates (Fig. 5a–c). The fresh vesuvianite samples were chosen for the polishing

of 100 μm-thickness laser sheets. Back-scattered electron (BSE) images of vesuvianite were produced by JSM-7800F field emission scanning electron microscope (FESEM) at the State Key Laboratory of Ore Deposit Geochemistry (SKLODG), Institute of Geochemistry, Chinese Academy of Sciences (CAS). These images were used to avoid inclusions and fractures during the LA-ICPMS analysis. All the subsequent analyses were also completed at SKLODG.

3.2.1. Major and trace elements

Electron microprobe analyses of major elements for vesuvianite and grossularite were performed on a JEOL JXA 8230 Electron Probe, and its specific experimental parameters are listed in Supplementary data S1.

The trace element concentrations were determined by LA-ICPMS using a Thermal Fisher Scientific Finnigan Element XR-ICPMS equipped with a GeoLasPro 193 nm ArF excimer laser. Each analysis was incorporated with a background acquisition of approximately 30 s followed by 50 s of data acquisition from the sample. Element contents were calibrated against multiple-reference materials (NIST 610 , NIST 612, BCR-2G, BIR-1G and BHVO-2G) with Si determined by EPMA as the
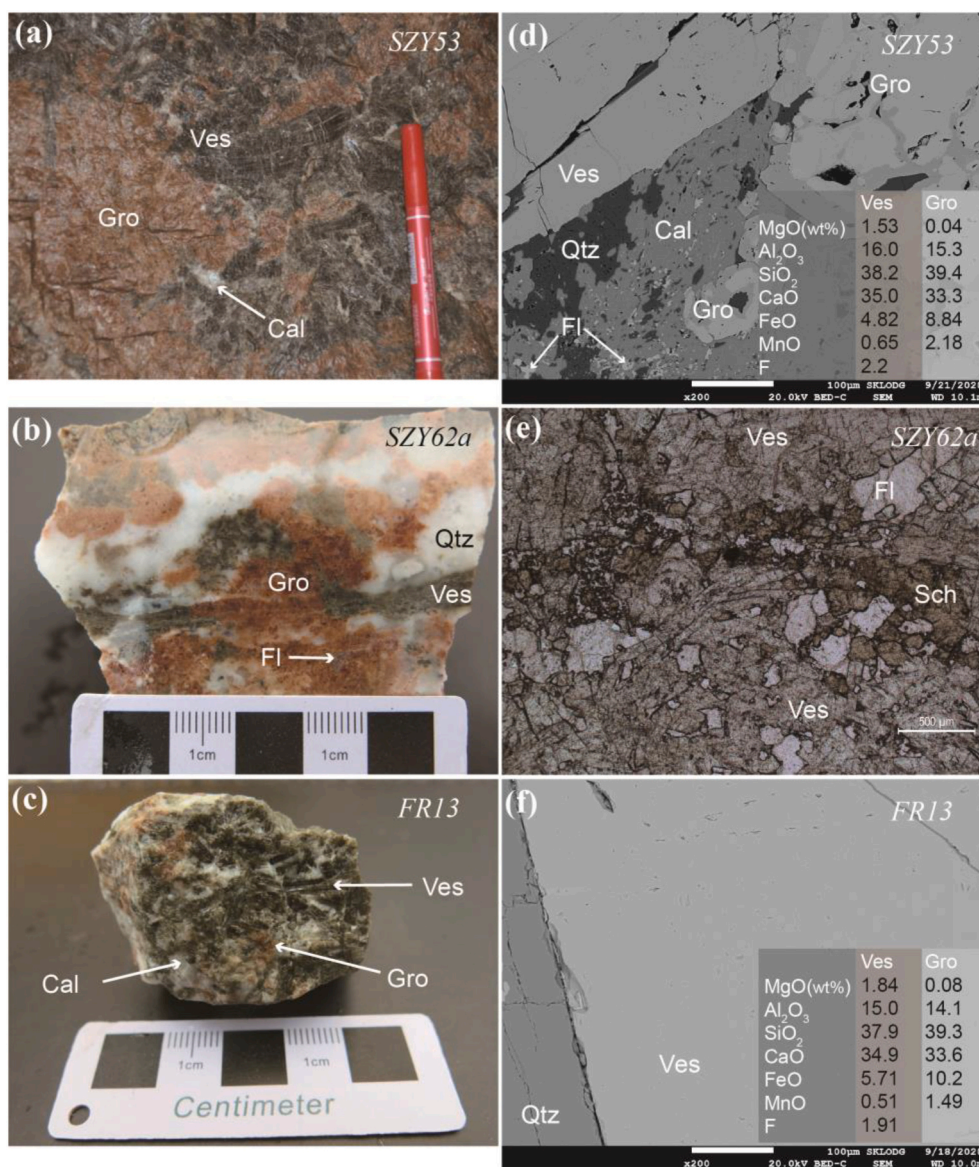

Fig. 5. Photographs (a, b and c) and backscattered electron (BSE) images (d, f) and photomicrograph (e) of vesuvianite samples from the Shizhuyuan W-Sn polymetallic deposit and the Furong Sn deposit. Major elements of vesuvianite and intergrown grossularite are also expressed in Fig. 5d and f. Abbreviations: Cal = calcite, Fl = fluorite, Gro = grossularite, Qtz = quartz, Ves = vesuvianite, Sch = scheelite.

internal standard for vesuvianite and garnet (Liu et al., 2008). Off-line selection and integration of background and analyzed analyte signals, and time-drift correction and quantitative calibration were performed by ICPMSDataCal (Liu et al., 2010).

3.2.2. Vesuvianite U-Pb dating

U-Pb isotopic compositions of vesuvianite samples were determined using a Thermal Fisher Scientific Finnigan Element XR-ICPMS equipped with a GeoLasPro 193 nm ArF excimer laser, and the detailed experimental parameters are listed in Supplementary data S1. A 44 μm spot size was used with an energy density of 5 J/cm^2 and a repetition rate of 5 Hz to minimize elemental fractionation (Chen et al., 2021; Tang et al., 2021). No matrix-matched vesuvianite U-Pb standards were available, thus the zircon standard 91500, with well calibrated U-Pb age of ca. 1062 Ma (Wiedenbeck et al., 1995) and negligible matrix effect for garnet U-Pb dating (Deng et al., 2017; Tang et al., 2021), were used in this study as the external calibration standards for the vesuvianite U-Pb dating. The garnet QC4 from the Qicun deposit was used as the secondary standard to monitor the precision and accuracy of the U-Pb dating results. The obtained $^{206}Pb/^{238}U$ age of 130.0 ± 0.7 Ma in this study is in good agreement with the previously determined date of ca. 130.0 Ma (Deng et al., 2017; Chen et al., 2021; Tang et al., 2021). The detailed data were listed in the Supplementary.

Prior to analysis, signal strength at ICPMS was tuned for maximum sensitivity while keeping ThO/Th ratio below 0.3% and U/Th ratio at ca. 1.0. In order to eliminate common Pb contamination from the sample surface, 4 to 5 pulses of pre-ablation were performed in each analysis. Each analysis included approximately 20 s background acquisition and the consequent approximately 30 s sample ablation acquisition. Both 91500 and QC04 were analyzed twice for every ten to fifteen analyses of the tested sample. Off-line selection and integration of background and analyzed signals, time-drift correction, and quantitative calibration for U-Pb isotopes were conducted using the ICPMSDataCal software (Liu et al., 2010). In order to reduce or even eliminate the down-hole fractionation effects, only the first 25 s ablation data (excluding the beginning 2 s) were adopted during our calculation. Only smooth signals were used to preclude the effect from fluid and mineral inclusions or fractures. Software Isoplot 4.15 was used to calculate U-Pb ages and draw the Tera–Wasserburg concordia diagram, data errors for isotopic ratios are listed at 1σ.

3.2.3. ^{207}Pb correction method

The ^{204}Pb correction is less than the ^{207}Pb correction in precision because of the higher counting and measurement error caused by the low abundance of ^{204}Pb and the isobaric interference of ^{204}Hg. In this study, the ^{207}Pb correction method was employed for Pb isotope correction, which has been widely used for dating relatively young samples with considerable common Pb concentrations (Williams, 1998). Here we commonly defined f_{206} as the fraction of common ^{206}Pb vs. total ^{206}Pb, which can be calculated from the following equation (Chew et al., 2011):

$$f_{206} = \frac{^{206}Pb_c}{^{206}Pb_{total}} = \frac{\left(^{207}Pb/^{206}Pb\right)_m - {}^{207}Pb^*/{}^{206}Pb^*}{\left(^{207}Pb/^{206}Pb\right)_c - {}^{207}Pb^*/{}^{206}Pb^*} \quad (1)$$

Then the radiogenic $^{206}Pb/^{238}U$ ($^{206}Pb^*/^{238}U$) can be calculated by (Chew et al., 2011):

$$^{206}Pb^*/{}^{238}U = (1 - f_{206}) * \left(^{206}Pb/^{238}U\right)_m \quad (2)$$

The ^{207}Pb-corrected $^{206}Pb/^{238}U$ ages can be obtained by:

$$Age = \frac{1}{\lambda}\ln\left(^{206}Pb^*/{}^{238}U + 1\right) \quad (3)$$

Where $\left(^{207}Pb/^{206}Pb\right)_m$ and $\left(^{206}Pb/^{238}U\right)_m$ stand for the measured ratios, $^{207}Pb^*/^{206}Pb^*$ is the expected radiogenic ratio for the inferred

age, and $\left(^{207}Pb/^{206}Pb\right)_c$ represents the common Pb ratio (the initial $^{207}Pb/^{206}Pb$ value).

The parameters needed for the ^{207}Pb-correction are acquired by plotting a regression line through the uncorrected data on a Tera–Wasserburg concordia plot, in which the y-intercept represents the initial $^{207}Pb/^{206}Pb$ value (Tera and Wasserburg, 1972; Frost et al., 2001; Chew et al., 2011, 2014), the lower intercept is the $^{238}U/^{206}Pb^*$ ratio, and the lower intercept age was usually considered as the formation time of those common lead-bearing minerals (e.g., Chew et al., 2011; Deng et al., 2017; Tang et al., 2021). In some cases, the uncorrected original data are too close to obtain a robust regression line, the accurate initial $^{207}Pb/^{206}Pb$ value is required to anchor the upper intercept, the approach adopted conventionally is involved in analyzing the Pb isotopic composition of a co-existing phase with a low U/Pb ratio, such as galena, K-feldspar or plagioclase, which preserves the initial Pb isotopic composition at the time of mineral crystallization (Williams, 1998; Chew et al., 2011). Subsequently, these individual ^{207}Pb-corrected $^{206}Pb/^{238}U$ ages can be used to calculate the weighted average age.

4. Results

4.1. Major and trace elements

Compositions of major elements for vesuvianite and coexisting grossularite are listed in Supplementary data S2 and illustrated in Fig. 5. Accordingly, vesuvianite and grossularite roughly share similar chemical composition. For example, in the sample SZY53, the average SiO_2 contents are determined at 38.2% for vesuvianite and 39.4% for grossularite, the average CaO contents are 35.0% for vesuvianite and 33.3% for grossularite, the average Al_2O_3 contents are 16.0% for vesuvianite and 15.3% for grossularite, the above three elemental components together can reach about 90% of the total element content. Among other minor components, vesuvianite displays higher MgO, fluorine and structural-H_2O contents, while grossularite shows relatively higher FeO$_{total}$ and MnO contents. The intergrown vesuvianite and grossularite in other samples also show similar compositional characteristics.

All the measured vesuvianite samples exhibit similar trace elements' characteristics, the detailed data are documented in Supplementary data S3 and plotted in Fig. 6. Unlike major elements, the trace elements' compositions in vesuvianite and coexisting grossularite display some obvious differences. For instance, all vesuvianite samples analyzed in this study are characterized by the LREE enrichment and HREE depletion (Fig. 6), however, all analyzed grossularite samples exhibit REE patterns with LREE depletion and HREE enrichment (Fig. 6). In addition, another apparent discrepancy between the vesuvianite and intergrown grossularite lies in the uranium concentrations, which are much higher in vesuvianite (up to thousands of times) than in grossularite (Fig. 6).

4.2. U-Pb geochronology

Uranium-lead isotope data for the analyzed vesuvianite samples are listed in Supplementary data S4 and illustrated as U-Pb diagrams in Fig. 7. The uranium concentrations in the detected vesuvianite vary from tens of ppm to hundreds of ppm. The analyzed data with different U and common Pb concentrations define a well mixing line in the Tera-Wasserburg concordia diagram, with most data distributed in the middle-lower part of the regression line; and the y-intercepts (ranging from 0.8319 to 0.8583), which represent the $^{207}Pb/^{206}Pb$ ratio for common Pb in the system, are consistent with common Pb ratios in galena and other low U/Pb minerals (0.8206 to 0.8694; Wang et al., 2011; Wu, 2016; Supplementary data S6) in the district. In general, precise ages were obtained for all the selected vesuvianite samples, with the maximum error of lower intercept age less than 2.2%.

In the Shizhuyuan deposit, four samples all yielded precise ages, which can be divided to three groups from the oldest to the youngest. The age of Sample SZY109 was the oldest, a total of 43 analyses
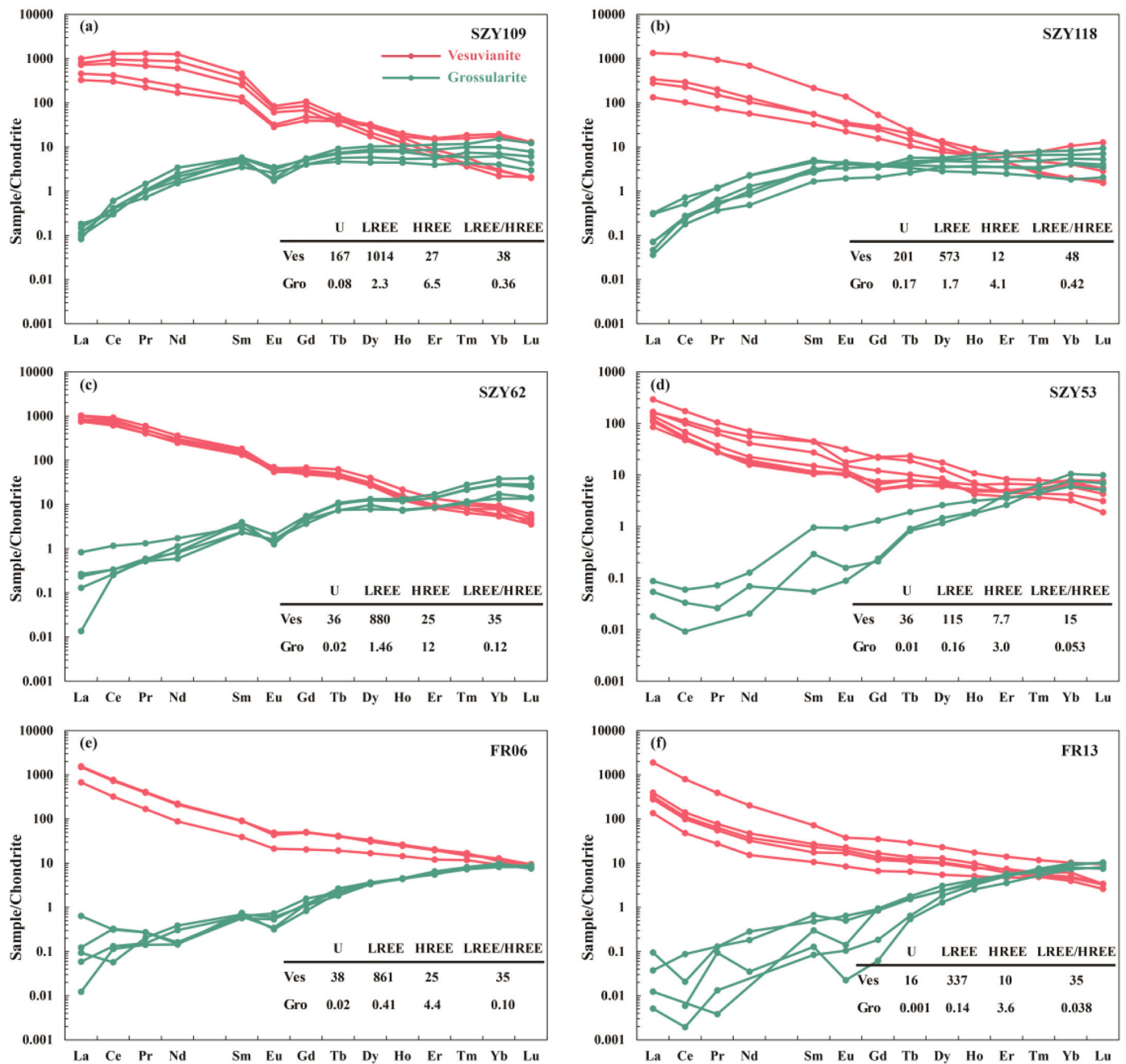
Fig. 6. REE characteristics and uranium concentrations of the vesuvianite and coexisting grossularite analyzed in this study. Chondrite normalized values are from Sun and McDonough (1989).

produced a lower intercept date of 160.3 ± 1.2 Ma (MSWD = 2.6, initial $^{207}Pb/^{206}Pb = 0.8371$) (Fig. 7a), and its ^{207}Pb-corrected data yielded a mean $^{206}Pb/^{238}U$ age of 160.5 ± 0.8 Ma (MSWD = 2.9, $n = 41$), 2 of 43 spots were rejected due to the inaccurate corrected U-Pb dates caused by high common Pb. Samples SZY118 and SZY62 obtained similar ages of ca. 155 Ma, Sample SZY118 yielded a lower intercept date of 155.6 ± 2.6 Ma (MSWD = 1.01, $n = 24$, initial $^{207}Pb/^{206}Pb = 0.8459$) (Fig. 7b) and a mean ^{207}Pb-corrected $^{206}Pb/^{238}U$ age of 155.4 ± 1.6 Ma (MSWD = 2.0, $n = 24$), Sample SZY62 produced a lower intercept date of 154.5 ± 3.1 Ma (MSWD = 1.3, $n = 24$, initial $^{207}Pb/^{206}Pb = 0.8583$) and a mean ^{207}Pb-corrected $^{206}Pb/^{238}U$ age of 154.1 ± 1.1 Ma (MSWD = 2.0, $n = 24$) (Fig. 7c). Sample SZY53 defined the youngest lower intercept date of 150.4 ± 3.3 Ma (MSWD = 1.8, $n = 42$, initial $^{207}Pb/^{206}Pb = 0.8477$) (Fig. 7d) and the mean ^{207}Pb-corrected $^{206}Pb/^{238}U$ age was calculated at 150.6 ± 1.5 Ma (MSWD = 2.9, 6 of 42 were rejected).

Two samples from the Furong deposit also yielded precise age data. Sample FR06 produced the older lower intercept date of 159.3 ± 1.8 Ma (MSWD = 2.5, $n = 78$, initial $^{207}Pb/^{206}Pb = 0.8319$) and a mean ^{207}Pb-corrected $^{206}Pb/^{238}U$ age of 157.9 ± 1.2 Ma (MSWD = 4.1, $n = 74$) (Fig. 7e). Sample FR13 produced the younger lower intercept age of 149.1 ± 1.6 Ma (MSWD = 1.05, $n = 41$, initial $^{207}Pb/^{206}Pb = 0.8413$), and the ^{207}Pb-corrected U-Pb data yielded a mean $^{206}Pb/^{238}U$ date of 148.3 ± 2.1 Ma (MSWD = 3.5, $n = 37$) (Fig. 7f).

5. Discussion

5.1. Comparison of the vesuvianite U-Pb ages with previously-published dates

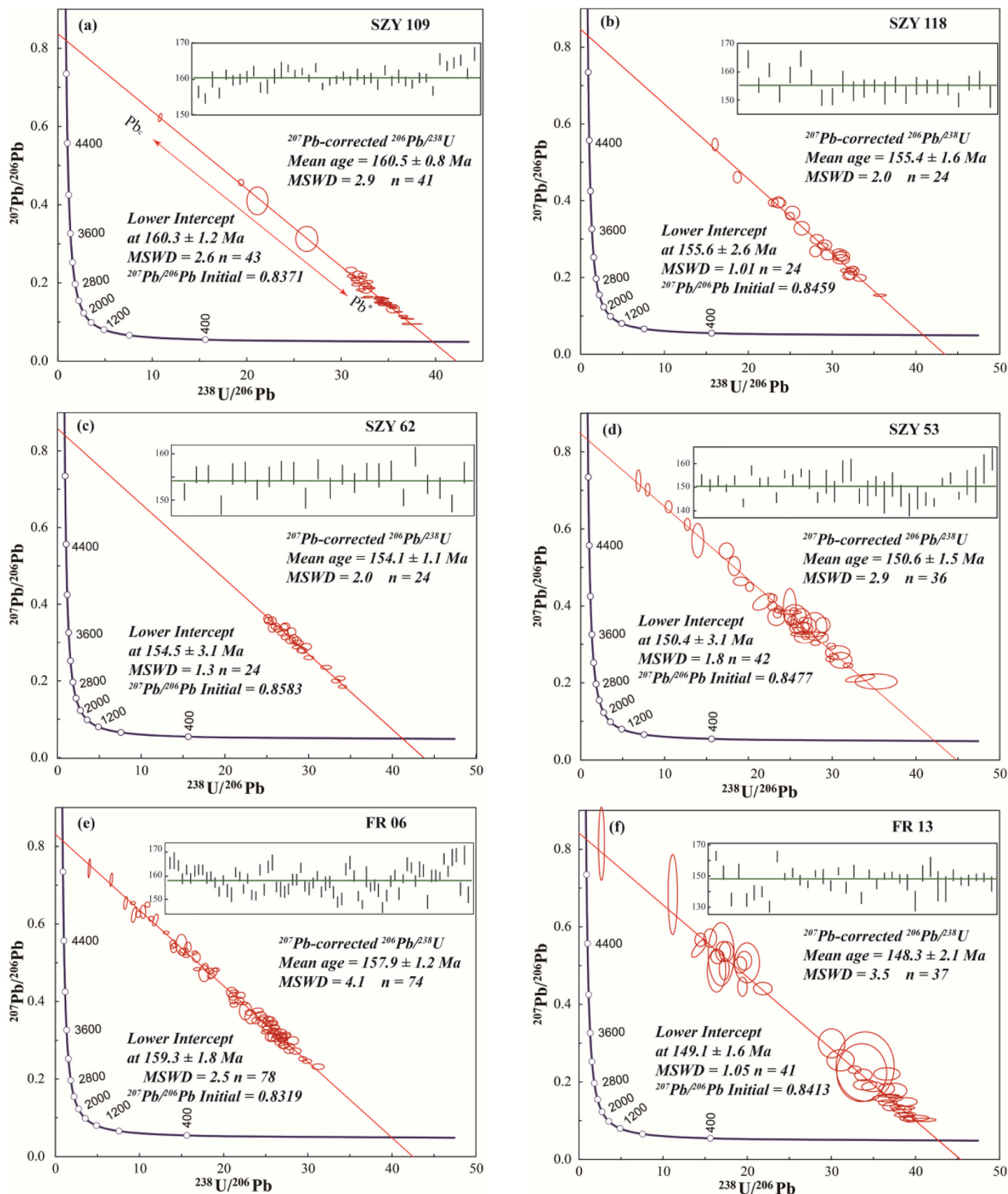As result, we have obtained six precise vesuvianite U-Pb ages, and all

Fig. 7. Tera-Wasserburg U-Pb plots, the lower intercept ages and ^{207}Pb-corrected mean ^{206}Pb/^{238}U ages of vesuvianite samples. Fig. 7a–d for the Shizhuyuan W-Sn polymetallic deposit, Fig. 7e and f for the Furong Sn deposit. Error ellipses and error bars are at the 1σ level.

these dates are consistent with previously published data dated on the corresponding granite and coexisting ores.

Sample SZY109 with the vesuvianite crystallization age of 160.3 ± 1.2 Ma was taken from the skarn occurring in the contact zone between the Devonian limestone and the first emplaced granite of the Qianlishan pluton (Fig. 2). Chen et al. (2014) determined an accurate zircon U-Pb age of 160.3 ± 1.1 Ma on this granite, moreover, Liu et al. (2012) successfully dated the Jinchuantang Sn-Bi deposit located in the contact zone of the western margin of this stage granite, and obtained a Re-Os age of 159.8 ± 2.9 Ma on molybdenite (Fig. 2).

Sample SZY62 with the age of 154.5 ± 3.1 Ma was collected from skarns in the Chaishan pit situated in the southern margin of the Qianlishan pluton (Fig. 2). The causative granite nearby was emplaced at 154.4 ± 0.9 Ma determined by the zircon U-Pb dating (Liao et al., 2021), and similar zircon U-Pb dates for this stage granite in other locations include 156 ± 1 Ma and 155 ± 2 Ma (Chen et al., 2014), 154.9 ± 0.8 Ma and 155.5 ± 1.4 Ma (Zhao et al., 2018). Noticeably, the muscovite samples collected from the greisen and skarn ores in this pit yielded consistent Ar-Ar ages of 155.5 ± 1.1 Ma and 156.8 ± 1.1 Ma (Zhao et al., 2018), and molybdenite from skarn also yielded a consistent age of 155.5 ± 1.4 Ma (Zhao et al., 2018). Sample SZY118 with the vesuvianite crystallization age of 155.6 ± 2.6 Ma was taken from the skarn formed by this stage granite in other location as shown in Fig. 2.

Sample SZY53 with the vesuvianite crystallization age of 150.4 ± 3.3 Ma was sampled from the 490 m level tunnel in the southeastern part of the Qianlishan pluton (Fig. 2). The nearby granite dykes were successfully dated by Jiang et al. (2019) with the zircon U-Pb ages of 151 ± 0.3 Ma and 152 ± 0.3 Ma (Fig. 3). Many similar mineralization dates had been obtained during the past 30 years, molybdenite from the mineralized skarn yielded a similar Re-Os isochron age of 151.0 ± 3.5 Ma (Li et al., 1996), those metasomatic minerals including garnet, fluorite and wolframite from skarn and greisen defined a Sm-Nd isochron age of 149 ± 2 Ma (Li et al., 2004), and Zhao et al. (2018) dated greisen with a muscovite Ar-Ar age of 151 ± 1 Ma. All the above dates are consistent with our result (150.4 ± 3.3 Ma) within error.

Sample FR06 with the vesuvianite crystallization age of 159.3 ± 1.8 Ma was taken from the skarn produced by the Qitianling pluton (Fig. 4), the emplacement time of the latter has been accurately determined at ca. 160 Ma by the zircon U-Pb method (Fu et al., 2004; Zhu et al., 2009). Yuan et al. (2011) dated cassiterite from the same orebody (No.19), which yielded the U-Pb ages of 159.9 ± 1.9 Ma by LA-ICPMS and 158.2 ± 0.4 Ma by ID-TIMS, respectively. Mao et al. (2004) and Peng et al. (2007) successfully dated the greisen tin ores in the adjacent Taoxiwo Mine by the mica Ar-Ar method respectively, and obtained similar dates of 160.6 ± 0.9 Ma and 159.9 ± 0.5 Ma (Fig. 4).

Sample FR13 collected from skarn ores in No.19 orebody yielded a precise age of 149.1 ± 1.6 Ma, a similar Ar-Ar age (150.6 ± 1 Ma) was determined by Peng et al. (2007) on phlogopite in skarn from the same orebody. The cassiterite taken from the adjacent mine also produced an approximate age of 151.9 ± 2.2 Ma (Carr et al., 2020). Notably, the above dates coincide well with the emplacement age of the third stage granite dated at ca. 149 Ma (Zhu et al., 2009).

To sum up, all of our vesuvianite dates are well consistent with the emplacement ages of the relevant granite and crystallization ages of other coexisting metasomatic rocks and/or minerals within error. Consequently, our dating results in this study are proved to be accurate and reliable, and multistage granite emplacement and hydrothermal mineralization events took place during the Mesozoic in the Nanling region, South China.

5.2. Substitution behavior of uranium and lead in vesuvianite

In recent years, U-Th-Pb dating of calcium-containing minerals (e.g., apatite, calcite, grandite, and vesuvianite in this study) has been widely applied, therefore, it is crucial to ascertain the behavior of the parent elements (uranium/thorium) in these minerals. Generally, uranium/

thorium are considered to replace calcium in these calcium-containing minerals due to their similar ion radius (e.g., Himmelberg and Miller, 1980; Moiseev et al., 2020). For example, the U/Th substitution of Ca could be expressed as $2Ca^{2+} \leftrightarrow U^{4+}/Th^{4+} + \square$ or $3Ca^{2+} \leftrightarrow U^{4+}/Th^{4+} + 2Na^{+}$ ($\square$ for vacancies or H_2O molecules) for vesuvianite (Moiseev et al., 2020), and $Ca^{2+} + 2Si^{4+} \leftrightarrow U^{4+} + 2(Fe^{3+}, Al^{3+})$ for grandite (Gaspar et al., 2008). But the geochemical behavior of uranium or thorium in these minerals remains enigmatic, e.g., there is no consensus on why andradite ($Ca_3Fe_2[SiO_4]_3$) usually can accommodate more uranium and is more suitable for U-Pb dating than grossularite ($Ca_3Al_2[SiO4]_3$) (Rák et al., 2011; Guo et al., 2016; Deng et al., 2017), although both minerals bear abundant Ca^{2+} in their lattice and are usually intergrown in nature. It is true for vesuvianite ($Ca_{10}(Mg, Fe)_2Al_4[SiO_4]_5[Si_2O_7]_2 (OH, F)_4$) and grossularite (Figs. 5 and 6).

As well known, the rare trace elements (REE) also substitute calcium in the above three minerals due to their similar ion radius, probably share same substitution mechanism with U and Th (e.g., Smith et al., 2004; Moiseev et al., 2020). However, grossularite, vesuvianite and andradite exhibit different REE patterns, grossularite is relatively enriched in HREE and markedly depleted in LREE (Fig. 6), while vesuvianite is characterized by LREE-enrichment and HREE-depletion (Fig. 6), and andradite usually accommodate more LREE than grossularite and share a similar REE pattern with vesuvianite (e.g., Deng et al., 2017; Zhang et al., 2019). In fact, the differences in HREE concentrations among the above three minerals aren't obvious, the different REE patterns mainly depend on their LREE concentrations. Both LREE and HREE share the same valence ($+3$) except Eu^{2+} and Ce^{4+}, therefore, the distinct differences between LREE and HREE predominantly lie in their ion radius, thus the different size of Ca^{2+} position in these minerals is likely to be the important factor controlling the accommodation capacity of LREE. In view of a more excellent positive linear correlation existed between uranium and LREE than HREE in andradite and vesuvianite (Fig. 8), and the extremely low uranium and LREE concentrations in HREE-rich grossularite (Fig. 6), it can be concluded that the substitution behavior of U^{4+} in these above calcium-bearing minerals should more resemble that of $LREE^{3+}$ than $HREE^{3+}$. Therefore, just like LREE, uranium concentrations are likely to be dependent upon the size of Ca^{2+} position in different minerals. In order to verify this conjecture, here we simply compare the structural parameters of Ca^{2+} (hereinafter X) in grossularite, andradite and vesuvianite.

Grossularite and andradite constitute the two end members of grandite ($Ca_3(Al, Fe)_2[SiO_4]_3$) and share the same fundamental crystal structure, but the former has a smaller lattice volume (Meagher, 1975; Ganguly, 1976; Armbruster and Geiger, 1993). There is only one type of eight-coordinated X-site in grandite, and the average interatomic distances of X-O are 2.406 Å for grossularite and 2.432 Å for andradite (Meagher, 1975; Armbruster and Geiger, 1993), respectively. Theoretically, the crystal structure of vesuvianite is derived from the grossularite orthosilicate structure but is more complex than this structure, specifically, there are two kinds of channels along its c axis in vesuvianite, one is similar to grossularite, and the other is different (Allen and Burnham, 1992; Lai et al., 2013). In contrast to grandite, there exist four types of X-site in vesuvianite, X_1 and X_4 are eight-coordinated with an average X-O distance of 2.443–2.453 Å and 2.495 Å, respectively; X_2 is seven-coordinated with an average X-O distance of 2.424–2.430 Å and X_3 is nine-coordinated with an average X-O distance of 2.578–2.584 Å (Moiseev et al., 2020). Obviously, the size of X_1-, X_3- and X_4-sites in vesuvianite is slightly larger than that of X-site (2.432 Å) in andradite, and significantly larger than that of X-site (2.406 Å) in grossularite, which makes vesuvianite accommodate similar or more uranium and LREE relative to andradite, and incorporate significantly more uranium and LREE than grossularite. Therefore, the differences in fine crystal structure among these minerals can well explain why grossularite and vesuvianite are usually intergrown in nature and share similar elemental components (Fig. 5), but display distinct differences in REE pattern and uranium concentrations (Fig. 6). It is true for grossularite and andradite.
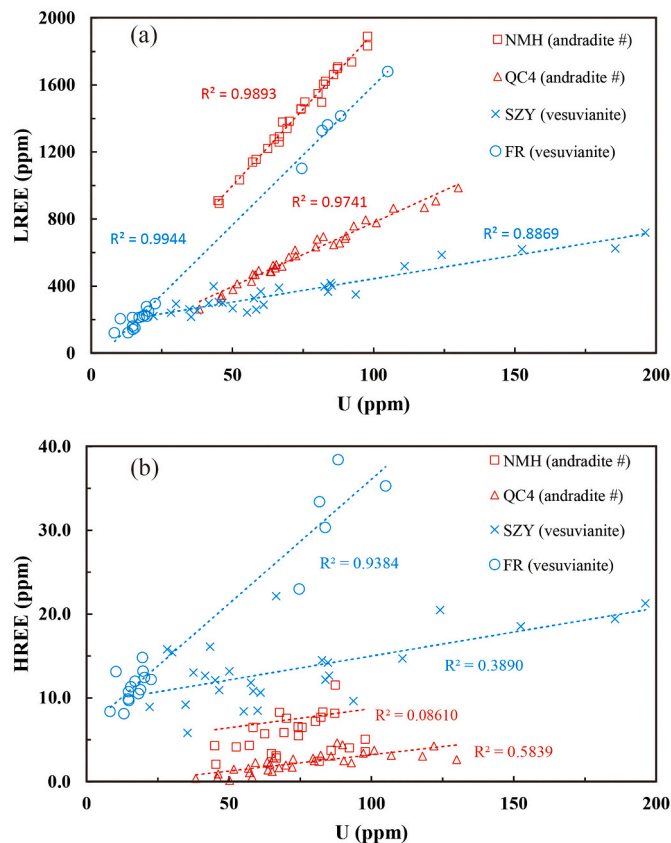
Fig. 8. Correlation between uranium concentrations and LREE (La-Eu), HREE (Gd-Lu) concentrations. R^2 represent correlation coefficient. Marked data andradite # are adopted from Deng et al. (2017).

Besides, the low capacity of uranium element in grossularite will also lead to an increase of uranium concentrations in the residual hydrothermal solution, and finally result in the uranium enrichment in vesuvianite and andradite.

Theoretically, a larger X position is also capable of incorporating more common Pb into the vesuvianite lattice, which is disadvantageous to the U-Pb dating. However, the common Pb concentrations of vesuvianite in this study are relatively low, since the parameter f_{206} (common Pb/total Pb) for most analyzed spots are less than 0.5, and the total Pb concentrations also are relatively low, usually in the range of several to a dozen ppm, therefore, the influences of common Pb upon our dating results can be negligible. The small dating errors (less than 2%) as shown in Fig. 7 can also lend support for this opinion. As far as the low concentrations of common Pb in vesuvianite is concerned, it is probably associated with the Pb^{2+} size, Pb^{2+} (e.g., eight-coordinated, 1.29 Å, Shannon, 1976) is obviously bigger than Ca^{2+} (1.12 Å, Shannon, 1976), which limits the substitution of Ca^{2+} by Pb^{2+} in quantity. It is worthwhile to mention that, the relatively high uranium concentrations in vesuvianite (tens to hundreds of ppm), to a large extent, also can diminish the negative effects caused by common Pb.

6. Conclusions

We have accurately dated six vesuvianite samples from two famous skarn deposits in South China using the in-situ LA-ICPMS U-Pb dating method. The main conclusions are obtained in this study as follows:

(1) Four vesuvianite samples from the Shizhuyuan deposit yielded precise ages of 160.3 ± 1.2 Ma, 155.6 ± 2.6 Ma, 154.5 ± 3.1 Ma and 150.4 ± 3.1 Ma, respectively. Two vesuvianite samples from the Furong deposit also obtained precise ages of 159.3 ± 1.8 Ma and 149.1 ± 1.6 Ma, respectively. These dates coincide well with the previously

published age data of the causative granite complex and the W-Sn mineralization. These results indicate that the vesuvianite U-Pb geochronometer can be applied to accurately date the skarnization process and skarn mineralization.

(2) The substitution behavior of U^{4+} into Ca^{2+} in vesuvianite more resembles that of LREE^{3+} than HREE^{3+}, vesuvianite can accommodate more uranium than intergrown grossularite and are beneficial for the U-Pb dating, and the influences of common Pb are negligible during the vesuvianite dating.

Declaration of Competing Interest

The authors declare that they have no known competing financial interests or personal relationships that could have appeared to influence the work reported in this paper.

Appendix A. Supplementary data

Supplementary data to this article can be found online at https://doi.org/10.1016/j.chemgeo.2022.121017.

References

Allen, F.M., Burnham, C.W., 1992. A comprehensive structure-model for vesuvianite: symmetry variations and crystal growth. Can. Mineral. 30, 1–18.
Armbruster, T., Geiger, C.A., 1993. Andradite crystal-chemistry dynamic X-site disorder and structure strain in silicate garnets. Eur. J. Mineral. 5, 59–71.
Cai, J.H., Wei, C.S., Sun, M.H., Wei, S.L., Huang, G.F., 2004. Ore-forming characteristics and prospecting significance of the Bailashui tin deposit in the Furong orefield. Geol. Explor. 40, 27–32 (in Chinese with English abstract).
Carr, P.A., Zink, S., Bennett, V.C., Norman, M.D., Amelin, Y., Blevin, P.L., 2020. A new method for U-Pb geochronology of cassiterite by ID-TIMS applied to the Mole Granite polymetallic system, eastern Australia. Chem. Geol. 539, 119539.
Chang, Z.S., Shu, Q.H., Meinert, L.D., 2019. Skarn deposits of China. In: Chang, Z.S., Goldfard, R.J. (Eds.), Mineral Deposits of China. Society of Economic Geologists, Littleton, pp. 189–234.
Chen, Y.C., Pei, R.F., Zhang, H.L., Lin, X.D., Bai, G., Li, C.Y., Hu, Y.J., Liu, G.Q., Xian, B. Q., 1989. The Geology of Non-Ferrous and Rare Metal Deposits Related to Mesozoic Granitoids in Nanling Region. The Geological Publishing House, Beijing, pp. 1–508 (in Chinese).
Chen, B., Ma, X.H., Wang, Z.Q., 2014. Origin of the fluorine-rich highly differentiated granites from the Qianlishan composite plutons (South China) and implications for polymetallic mineralization. J. Asian Earth Sci. 93, 301–314.
Chen, Y.X., Li, H., Sun, W.D., Ireland, T., Tian, X.F., Hu, Y.B., Yang, W.B., Chen, C., Xu, D. R., 2016. Generation of late Mesozoic Qianlishan A 2 -type granite in Nanling Range, South China: implications for Shizhuyuan W-Sn mineralization and tectonic evolution. Lithos. 266, 435–452.
Chen, Y.H., Hu, R.Z., Lan, T.G., Wang, H., Tang, Y.W., Yang, Y.H., Tian, Z.D., Ulrich, T., 2021. Precise U Pb dating of grandite garnets by LA-ICP-MS: assessing ablation behaviors under matrix-matched and non-matrix-matched conditions and applications to various skarn deposits. Chem. Geol. 572, 120198.
Chew, D.M., Sylvester, P.J., Tubrett, M.N., 2011. U-Pb and Th-Pb dating of apatite by LA-ICPMS. Chem. Geol. 280, 200–216.
Chew, D.M., Petrus, J.A., Kamber, B.S., 2014. U-Pb LA-ICPMS dating using accessory mineral standards with variable common Pb. Chem. Geol. 363, 185–199.
Deng, X.D., Li, J.W., Luo, T., Wang, H.Q., 2017. Dating magmatic and hydrothermal processtases using andradite-rich garnet U–Pb geochronometry. Contrib. Mineral. Petrol. 172, 70–81.
Einaudi, M.T., Burt, D.M., 1982. Introduction, terminology, classification, and composition of skarn deposits. Econ. Geol. 77, 745–754.
Frost, B.R., Chamberlain, K.R., Schumacher, J.C., 2001. Sphene (titanite): phase relations and role as a geochronometer. Chem. Geol. 172, 131–148.

Fu, J.M., Ma, C.Q., Xie, C.F., Zhang, Y.M., Peng, S.B., 2004. Zircon SHRIMP dating of the Cailing granite on the eastern margin of the Qitianling granite, Hunan, South China, and its significance. Geol. China 31, 96–100 (in Chinese with English abstract).

Ganguly, J., 1976. The energetic of nature garnet solid solution. II. Mixing of the calcium silicate end-members. Contrib. Mineral. Petrol. 55, 81–90.

Gaspar, M., Knaack, C., Meinert, L.D., Moretti, R., 2008. REE in skarn systems: a LA-ICP-MS study of garnets from the Crown Jewel gold deposit. Geochim. Cosmochim. Acta 72, 185–205.

Gulson, B.L., Jones, M.T., 1992. Cassiterite: potential for direct dating of mineral deposits and a precise age for the Bushveld complex granites. Geology 20, 355–358.

Guo, C., Wang, R., Yuan, S., Wu, S., Yin, B., 2015. Geochronological and geochemical constraints on the petrogenesis and geodynamic setting of the Qianlishan granitic pluton Southeast China. Mineral. Petrol. 109, 253–282.

Guo, X.F., Navrotsky, A., Kukkadapu, R.K., Engelhard, M.H., Lanzirotti, A., Newville, M., Ilton, E.S., Sutton, S.R., Xu, H.W., 2016. Structure and thermodynamics of uranium-containing iron garnets. Geochim. Cosmochim. Acta 189, 269–281.

Himmelberg, G.R., Miller, T.P., 1980. Uranium- and thorium-rich vesuvianite from the Seward Peninsula, Alaska. Am. Mineral. 65, 1020–1025.

Huang, G.F., Zeng, Q.W., Wei, S.L., Xu, Y.M., Kang, W.J., 2001. Geological characteristics and ore-controlling factors of the Furong orefield, Qitianling, Hunan. Chin. Geol. 28, 30–34 (in Chinese).

Jiang, W.C., Li, H., Mathur, R., Wu, J.H., 2019. Genesis of the giant Shizhuyuan W-Sn–Mo–Bi–Pb–Zn polymetallic deposit, South China: constraints from zircon geochronology and geochemistry in skarns. Ore Geol. Rev. 111, 103160.

Lai, X.J., Zhu, F., Li, Y.C., Liu, J., Wu, X., 2013. Compressibility of a natural *P4/nnc* vesuvianite. Eur. J. Mineral. 25, 631–637.

Li, H.Y., Mao, J.W., Sun, Y.L., Zou, X.Q., He, H.L., Du, A.D., 1996. Re–Os isotopic chronology of molybdenites in the Shizhuyuan polymetallic tungsten deposit, Southern Hunan. Geol. Rev. 42, 261–267 (in Chinese).

Li, X.H., Liu, D.Y., Sun, M., Li, W.X., Liang, X.R., Liu, Y., 2004. Precise Sm–Nd and U–Pb isotopic dating of the supergiant Shizhuyuan polymetallic deposit and its host granite, SE China. Geol. Mag. 141, 225–231.

Li, J.D., Bai, D.Y., Wu, G.Y., 2005. Zircon SHRIMP dating of the Qitianling granite, Chenzhou, southern Hunan, and its geological significance. Geol. Bull. China 24 (5), 411–414 (in Chinese).

Li, H.Q., Lu, Y.F., Wang, D.H., Chen, Y.C., Yang, H.M., Guo, J., Xie, C.F., Mei, Y.P., Ma, L. Y., 2006. Dating of the rock-forming and ore-forming ages and their geological significances in the Furong ore-field, Qitian Mountain, Hunan. Geol. Rev. 52, 114–121 (in Chinese with English abstract).

Liao, Y.Z., Zhao, B., Zhang, D.H., Danyushevsky, L.V., Li, T.L., Wu, M.Q., Liu, F., 2021. Evidence for temporal relationship between the late Mesozoic multistage Qianlishan granite complex and the Shizhuyuan W–Sn–Mo–Bi deposit, SE China. Sci. Rep. 11, 5828.

Liu, Y.M., Tai, D.M., Lu, H.Z., Xu, Y.Z., Wang, C.L., Kang, W.Q., 1997. ^{40}Ar-^{39}Ar and Sm-Nd isotope age of Qianlishan granite and mineralization. Sci. China Ser. D 27, 426–430 (in Chinese).

Liu, Y.S., Hu, Z.C., Gao, S., Günther, D., Xu, J., Gao, C.G., Chen, H.H., 2008. In situ analysis of major and trace elements of anhydrous minerals by LA-ICP-MS without applying an internal standard. Chem. Geol. 257, 34–43.

Liu, Y.S., Hu, Z.C., Zong, K.Q., Gao, C.G., Gao, S., Xu, J., Chen, H.H., 2010. Reappraisal and refinement of zircon U–Pb isotope and trace element analyses by LA-ICP-MS. Chin. Sci. Bull. 55, 1535–1546.

Liu, X.F., Yuan, S.D., Wu, S.H., 2012. Re-Os dating of the molybdenite from the Jinchantang tin-bismuth deposit in Huannan Province and its geological significance. Acta Petrol. Sin. 28, 39–51 (in Chinese with English abstract).

Lu, H.Z., Liu, Y.M., Wang, C.L., Xu, Y.Z., Li, H.Q., 2003. Mineralization and fluid inclusion study of the Shizhuyuan W-Sn-Bi-Mo-F skarn deposit, Hunan province, China. Econ. Geol. 98, 955–974.

Luck, J.M., Allègre, C.J., 1982. The study of molybdenites through the ^{187}Re-^{187}Os chronometer. Earth Planet. Sci. Lett. 61, 291–296.

Mao, J.W., Li, H.Y., Hidehiko, S., Louis, R., Bernard, G., 1996. Geology and metallogeny of the Shizhuyuan skarn-greisen deposit, Hunan province, China. Int. Geol. Rev. 38, 1020–1039. https://doi.org/10.1080/00206819709465379.

Mao, J.W., Li, X.F., Chen, W., Lan, X.M., Wei, S.L., 2004. Geological characteristics of the Furong tin orefield, Hunan, ^{40}Ar–^{39}Ar dating of tin ores and related granite and its geodynamic significance for rock and ore formation. Acta Petrol. Sin. (Engl. Ed.) 78, 481–491.

Mao, J.W., Xie, G.Q., Guo, C.L., 2007. Large-scale tungsten-tin mineralization in the Nanling region, South China: metallogenic ages and corresponding geodynamic processes. Acta Petrol. Sin. 23, 2329–2338 (in Chinese with English abstract).

Mao, J.W., Cheng, Y.B., Chen, M.H., Pirajno, F., 2013. Major types and time-space distribution of Mesozoic ore deposits in South China and their geodynamic settings. Mineral. Deposita 48, 267–294. https://doi.org/10.1007/s00126-012-0446-z.

Mathur, R., Ruiz, J., Tornos, F., 1999. Age and sources of the ore at Tharsis and Rio Tinto, Iberian Pyrite Belt, from Re-Os isotopes. Mineral. Deposita 34, 790–793.

Meagher, E.P., 1975. The crystal structures of pyrope and grossularite at elevated temperatures. Am. Mineral. 60, 218–228.

Meinert, L.D., Dipple, G.M., Nicolescu, S., 2005. World skarn deposits. Econ. Geol. 299–336. Volume 100th Anniversary.

Moiseev, M.M., Panikorovskii, T.L., Aksenov, S.M., Mazur, A.S., Mikhailova, J.A., Yakovenchuk, V.N., Bazai, A.V., Ivanyuk, G.Y., Agakhanov, A.A., Shilovskikh, V.V., Pekov, I.V., Kasatkin, A.V., Rusakov, V.S., Yapaskurt, V.O., Karpenko, V.Y., Krivovichev, S.V., 2020. Insights into crystal chemistry of the vesuvianite-group: manaevite-(Ce), a new mineral with complex mechanisms of its hydration. Phys. Chem. Miner. 47, 17–31.

Peng, J.T., Zhou, M.F., Hu, R.Z., Shen, N.P., Yuan, S.D., Bi, X.W., Du, A.D., Qu, W.J., 2006. Precise molybdenite Re–Os and mica Ar–Ar dating of the Mesozoic Yaogangxian tungsten deposit, central Nanling district, South China. Mineral. Deposita 41, 661–669.

Peng, J.T., Hu, R.Z., Bi, X.W., Dai, T.M., Li, X.M., Shuang, Y., Yuan, S.D., Liu, S.R., 2007. ^{40}Ar/^{39}Ar isotopic dating of tin mineralization in Furong deposit of Hunan Province and its geological significance. Mineral. Deposita 26, 237–248 (in Chinese with English abstract).

Peng, J.T., Hu, R.Z., Yuan, S.D., Bi, X.W., Shen, N.P., 2008. The time ranges of granitoid emplacement and related nonferrous metallic mineralization in southern Hunan. Geol. Rev. 54, 617–625 (in Chinese with English abstract).

Rák, Z., Ewing, R.C., Becker, U., 2011. Role of iron in the incorporation of uranium in ferric garnet matrices. Phys. Rev. B 84, 155128. https://doi.org/10.1103/PhysRevB.84.155128.

Romer, R.L., 1992. Vesuvianite-new tool for the U-Pb dating of skarn ore deposits. Mineral. Petrol. 46, 331–341.

Seman, S., Stockli, D.F., McLean, N.M., 2017. U-Pb geochronology of grossular-andradite garnet. Chem. Geol. 460, 106–116.

Shannon, R.D., 1976. Revised effective ionic radii and systematic studies of interatomic distances in halides and chalcogenides. Acta Crystallogr. A32, 751–767.

Shu, L.S., Zhou, X.M., Deng, P., Yu, X.Q., 2006. Principal geological features of Nanling tectonic belt, South China. Geol. Rev. 52, 269–287 (in Chinese with English abstract).

Shu, L.S., Chen, X.Y., Lou, F.S., 2020. Pre-Jurassic tectonics of the South China. Acta Geol. Sin. 94 (2), 333–360 (in Chinese with English abstract).

Smith, M.P., Henderson, P., Jeffries, T.E.R., Long, J., Williams, C.T., 2004. The rare earth elements and uranium in garnets from the Beinnan Dubhaich aureole, Skye, Scotland, UK: constraints on processes in a dynamic hydrothermal system. J. Petrol. 45, 467–484.

Stein, H.J., Morgan, J.W., Schersten, A., 2000. Re-Os dating of low-level highly radiogenic (LLHR) sulfides: the Harnas Gold Deposit, Southwest Sweden, records continental-scale tectonic events. Econ. Geol. 95, 1657–1671.

Sun, S.S., McDonough, W.F., 1989. Chemical and isotopic systematics of oceanic basalt: implications for mantle composition and processes. In: Saunders, A.D., Norry, M.J. (Eds.), Magmatism in the Ocean Basins, pp. 313–345.

Tang, Y.W., Gao, J.F., Lan, T.G., Cui, K., Han, J.J., Zhang, X., Chen, Y.W., Chen, Y.H., 2021. In situ low-U garnet U-Pb dating by LA-SF-ICP-MS and its application in constraining the origin of Anji skarn system combined with Ar-Ar dating and Pb isotopes. Ore Geol. Rev. 130, 103970.

Tera, F., Wasserburg, G.J., 1972. U-Th-Pb systematics in three Apollo 14 basalt and the problem of initial Pb in lunar rocks. Earth Planet. Sci. Lett. 14, 281–304.

Tilton, G.R., Grünenfelder, M.H., 1968. Sphene: uranium-lead ages. Science 159, 1458–1461.

Wang, C.L., Luo, R.H., Xu, Y.Z., Sun, Y.H., Xie, C.G., Zhang, C.M., Xu, W.G., Ren, X.M., 1987. Geology of the Shizhuyuan Tungsten-Polymetallic Deposit. Geology Publish House, Beijing (in Chinese).

Wang, Q., Xu, W.X., Zeng, N.S., 2011. The Pb isotope geochemistry of Shizhuyuan deposit, Hunan Province. Acta Mineral. Sin. 31 (S1), 645–646 (in Chinese).

Wang, D.H., Huang, F., Wang, Y., He, H.H., Li, X.M., Liu, X.X., Sheng, J.F., Liang, T., 2020. Regional metallogeny of Tungsten-tin-polymetallic deposits in Nanling region, South China. Ore Geol. Rev. 120, 103305.

Wei, Q.D., Yang, M., Romer, R.L., Wang, H., Yang, Y.H., Zhao, Z.F., Wu, S.T., Xie, L.W., Huang, C., Xu, L., Yang, J.H., Wu, F.Y., 2022. In situ U–Pb geochronology of vesuvianite by LA-SF-ICP-MS. J. Anal. At. Spectrom. 37, 69–81.

Wiedenbeck, M., AllÉ, P., Corfu, F., Griffin, W.L., Meier, M., Oberli, F., Quadt, A.V., Roddick, J.C., Spiegel, W., 1995. Three natural zircon standards for U-Th-Pb, Lu-Hf, trace element and REE analyses. Geostand. Geoanal. Res. 19, 1–23.

Williams, I.S., 1998. U–Th–Pb geochronology by ion microprobe. In: McKibben, M.A., Shanks III, W.C., Ridley, W.I. (Eds.), Applications of Microanalytical Techniques to Understanding Mineralizing Processes, 7, pp. 1–35. Reviews in Economic Geology.

Wu, S.H., 2016. The Metallogenic Mechanism of Distal Contact Pb-Zn-Ag Veins in Shizhuyuan Ore District, Hunan Province, China. Doctor Degree Thesis, 618. China University of Geoscience, Beijing, pp. 4–52 (in Chinese).

Yu, G., Yang, G., Chen, J.F., Qu, W.J., Du, A.D., He, W., 2005. Re-Os dating of gold-bearing arsenopyrite from the Maoling gold deposit, Liaoning Province, Northeast China and its geological significance. Chin. Sci. Bull. 50, 1509–1514.

Yuan, S.D., Peng, J.T., Hao, S., Li, H.M., Geng, J.Z., Zhang, D.L., 2011. In situ LA-MC-ICP-MS and ID-TIMS U–Pb geochronology of cassiterite in the giant Furong tin deposit, Hunan Province, South China: new constraints on the timing of tin–polymetallic mineralization. Ore Geol. Rev. 43, 235–242.

Zhang, G.W., Guo, A.L., Wang, Y.J., 2013. Tectonics of South China continent and its implications. Sci. China Earth Sci. 56, 1804–1828 (in Chinese with English abstract).

Zhang, S.T., Chen, H.Y., Shu, Q.H., Zhang, Y., Chu, G.B., Cheng, J.M., Tian, J., 2019. Unveiling growth histories of multi-generational garnet in a single skarn deposit via newly-developed LA-ICP-MS U-Pb dating of grandite. Gondwana Res. 73, 65–76.

Zhao, K.D., Jiang, S.Y., Jiang, Y.H., Liu, D.Y., 2006. SHRIMP U–Pb dating of the Furong unit of Qitianling granite from southeast Hunan Province and their geological implications. Acta Petrol. Sin. 22 (10), 2611–2616 (in Chinese with English abstract).

Zhao, P.L., Yuan, S.D., Mao, J.W., Yuan, Y.B., Zhao, H.J., Zhang, D.L., Shuang, Y., 2018. Constraints on the timing and genetic link of the large-scale accumulation of proximal W-Sn-Mo-Bi and distal Pb-Zn-Ag mineralization of the world-class Dongpo orefield, Nanling Range, South China. Ore Geol. Rev. 95, 1140–1160.

Zhu, J.C., Wang, R.C., Zhang, P.H., Xie, C.F., Zhang, W.L., 2009. Zircon U-Pb geochronological framework of Qitianling granite batholith, middle part of Nanling range, South China. Sci. China Ser. D Earth Sci. 52, 1279–1294.